PNAS Nexus, 2024, 3, 1–9
https://doi.org/10.1093/pnasnexus/pgae079
Advance access publication 14 February 2024
Research Report

Quantitative description of the phase-separation behavior of the multivalent SLP65–CIN85 complex

Joachim Maier[a], Daniel Sieme[a], Leo E. Wong[a], Furqan Dar[b], Jürgen Wienands[c], Stefan Becker[a] and Christian Griesinger[a,*]

[a]Department of NMR Based Structural Biology, Max Planck Institute (MPI) for Multidisciplinary Sciences, 37077 Göttingen, Germany
[b]Department of Biomedical Engineering, Washington University in St Louis, St Louis, MO 63130, USA
[c]Institute of Cellular and Molecular Immunology, University Medical Center Göttingen, 37073 Göttingen, Germany
*To whom correspondence should be addressed: Email: cigr@mpinat.mpg.de
Edited By: Gerhard Hummer

Abstract

Biomolecular condensates play a major role in cell compartmentalization, besides membrane-enclosed organelles. The multivalent SLP65 and CIN85 proteins are proximal B-cell antigen receptor (BCR) signal effectors and critical for proper immune responses. In association with intracellular vesicles, the two effector proteins form phase separated condensates prior to antigen stimulation, thereby preparing B lymphocytes for rapid and effective activation upon BCR ligation. Within this tripartite system, 6 proline-rich motifs (PRMs) of SLP65 interact promiscuously with 3 SH3 domains of the CIN85 monomer, establishing 18 individual SH3–PRM interactions whose individual dissociation constants we determined. Based on these 18 dissociation constants, we measured the phase-separation properties of the natural SLP65/CIN85 system as well as designer constructs that emphasize the strongest SH3/PRM interactions. By modeling these various SLP65/CIN85 constructs with the program LASSI (LAttice simulation engine for Sticker and Spacer Interactions), we reproduced the observed phase-separation properties. In addition, LASSI revealed a deviation in the experimental measurement, which was independently identified as a previously unknown intramolecular interaction. Thus, thermodynamic properties of the individual PRM/SH3 interactions allow us to model the phase-separation behavior of the SLP65/CIN85 system faithfully.

Keywords: SLP65, BLNK, CIN85, phase separation, biomolecular condensates

Significance Statement

Biomolecular phase separation plays an important role in cellular organization. On the molecular level, phase separation is mediated by specific amino acid sequences, as they occur in intrinsically disordered proteins (IDPs) or low-complexity domains or by protein motifs/domains within multivalent proteins. Here, we study the proteins SLP65 and CIN85, which together with vesicles form a condensate in B-cells. SLP65 engages its six proline-rich motifs, which interact with the three SH3 domains of CIN85. We parameterized a thermodynamic computational model and described quantitatively the phase separation originating from the underlying individual interactions of SLP65 and CIN85 was using the software LASSI. LASSI faithfully revealed the determinants of phase separating these multivalent proteins.

Introduction

Liquid–liquid phase separation of biomolecules has emerged as a general principle for cellular organization (1, 2). A diverse set of biomolecules can participate in phase separation, e.g. intrinsically disordered proteins (IDPs) (3–7), proteins with low-complexity segments (8), RNA (9), or RNA-binding proteins (10), multivalent proteins (11) as well as synaptic vesicles (12). Phase separation has been described to regulate intracellular signaling pathways such as those engaged by the antigen receptors on B- and T-cells (13–16). The Src homology 2 domain-containing leukocyte protein of 65 kDa (SLP65) (17), also referred to as B-cell linker protein (BLNK) (18), orchestrates the intracellular signaling pathways of the B-cell antigen receptor (BCR), and exists in constitutive association with Cbl-interacting protein of 85 kDa (CIN85) (19, 20). Any interference with the expression of or association between SLP65 and CIN85 compromises human antibody responses (21–23). In resting B-cells, CIN85 and vesicle-associated SLP65 phase-separate into steady-state condensates, which facilitate and promote B-cell responsiveness to antigen encounter (14). The assembly of these phase-separated presignaling condensates is driven by the binding of SLP65's N-terminus to highly-curved cytosolic vesicles (19), as well as the promiscuous interaction of SLP65's proline-rich motifs (PRMs) with the three SH3 domains of CIN85 (14) and the trimerization of CIN85 by its coiled-coil (CC) domain (24) (Fig. 1A).

Competing Interest: The authors declare no competing interest.
Received: November 27, 2023. **Accepted:** February 6, 2024
© The Author(s) 2024. Published by Oxford University Press on behalf of National Academy of Sciences. This is an Open Access article distributed under the terms of the Creative Commons Attribution License (https://creativecommons.org/licenses/by/4.0/), which permits unrestricted reuse, distribution, and reproduction in any medium, provided the original work is properly cited.

Downloaded from https://academic.oup.com/pnasnexus/article/3/3/pgae079/7607901 by Max-Planck Society user on 21 March 2024

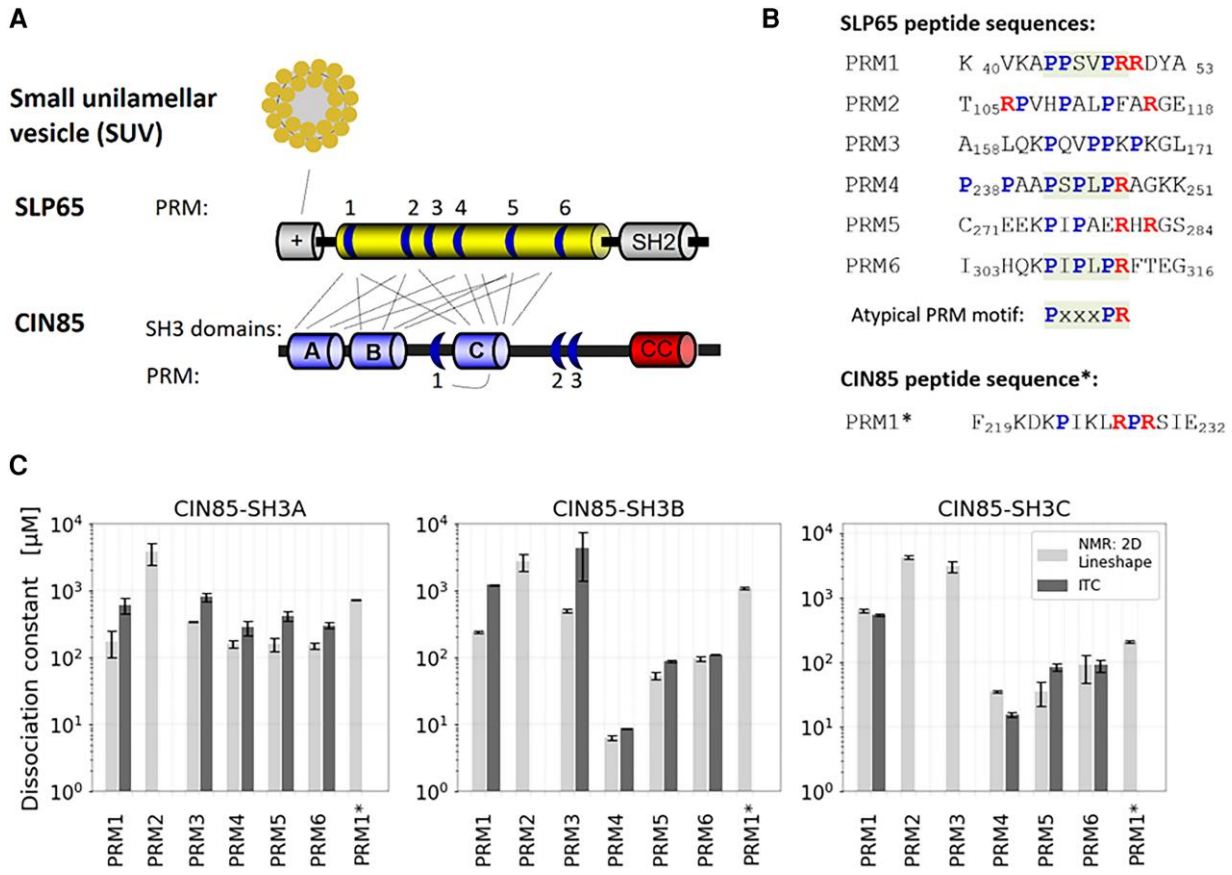

Fig. 1. A) Schematic illustration of the interactions mediating tripartite phase-separation of SLP65, CIN85, and SUVs. SLP65's positively charged N-terminus interacts with small unilamellar vesicles (SUVs) (14), while the C-terminal SH2 domain and numerous tyrosine phosphorylation motifs (not shown) conduct signal transduction (20, 25). SLP65's intrinsically disordered region (yellow) harbors six PRMs (blue regions), which promiscuously interact with the SH3A, SH3B, and SH3C domains of CIN85 (14). CIN85's CC domain forms a trimer (not shown). Additionally, CIN85's PRM1 interacts with SH3C (26). B) Overview of the sequences of the synthesized 14 amino acid long peptides derived from PRM regions. The atypical motif PxxxPR is highlighted in gray; Arg and Pro are colored red and blue, respectively. PRM1*, PRM1 of CIN85. C) Dissociation constants of single PRM-representing peptides to CIN85's SH3A, SH3B and SH3C domains. K_D values for PRM1* were provided by (D). Sieme (26). The 21 dissociation constants (K_Ds) of the SH3–PRM interactions range from 6 μM to ~4 mM. K_Ds were obtained by NMR (TITAN v1.5-3-g3566 (27) gray bars) and ITC titrations (black bars). Both methods show that PRM4 has the largest and second largest K_D in the interaction with SH3B and SH3C, respectively. No heat release was measured for the weak interactions of PRM2 with any SH3 domain and PRM3 with SH3C, thus no K_D is shown here.

The PRM_m–$SH3_n$ system is a prominent example of phase separation of multivalent proteins. Pioneering biophysical and computational studies worked with identical PRM and SH3 domains (28), yet, in SLP65 and CIN85 the six PRMs and the three SH3 domains differ in sequence (Fig. 1B). Therefore, the individual dissociation constants are expected to vary. Our approach is to relate the phase-separation properties to individual modules of SLP65 and CIN85. As a first step, the dissociation constants were measured. In the next step, the phase separation was modeled based on the ranking of the underlying SH3–PRM interactions by using the open-source program LASSI (29). LASSI can be used to describe the phase-separation properties of any sticker-spacer system. The program is geared toward multivalent proteins by implementing a lattice-based, coarse-grained Monte Carlo simulation. Previous phase-separation models of LASSI correlated phase-separation properties with the interaction strengths of individual amino acids with each other implemented as an energy matrix (30). In the herein-applied LASSI model, we interpreted each SH3 domain and each PRM as a single sticker and calibrated the linker lengths with the diameter of the SH3 domains. Isothermal phase diagrams were constructed by running a set of simulations of the binary mixtures, setting up different combinations of SLP65 and CIN85 constructs and their mutants. The constructs were also investigated experimentally, revealing a good correlation between the experimentally measured and simulated saturation concentrations. We arrive at a descriptive LASSI model for the CIN85–SLP65 system, reproducing the experimental observations quantitatively.

Results and discussion

Disentanglement of the promiscuous SH3–PRM interactions reveals the particular strong interaction of SLP65-PRM4 with CIN85's SH3B domain

In order to elucidate the thermodynamics of phase separation upon SLP65 and CIN85 condensate formation, the dissociation constants (K_Ds) of the underlying SH3–PRM interactions were measured. The 18 known interactions stemming from the three SH3 domains of CIN85 SH3A, SH3B, SH3C, and the six PRMs of SLP65 (Fig. S8 in Wong et al. (14)) were investigated by titrations. The K_Ds of the binary interactions were obtained from concentration-dependent chemical shift changes by NMR spectroscopy (Fig. 1C; SI Appendix, Figs. S1 and S2). Among the 18 titration experiments, the NMR resonances appeared in fast, slow, and intermediate exchange regimes (SI Appendix, Fig. S3). For illustration, the NMR

Downloaded from https://academic.oup.com/pnasnexus/article/3/3/pgae079/7607901 by Max-Planck Society user on 21 March 2024

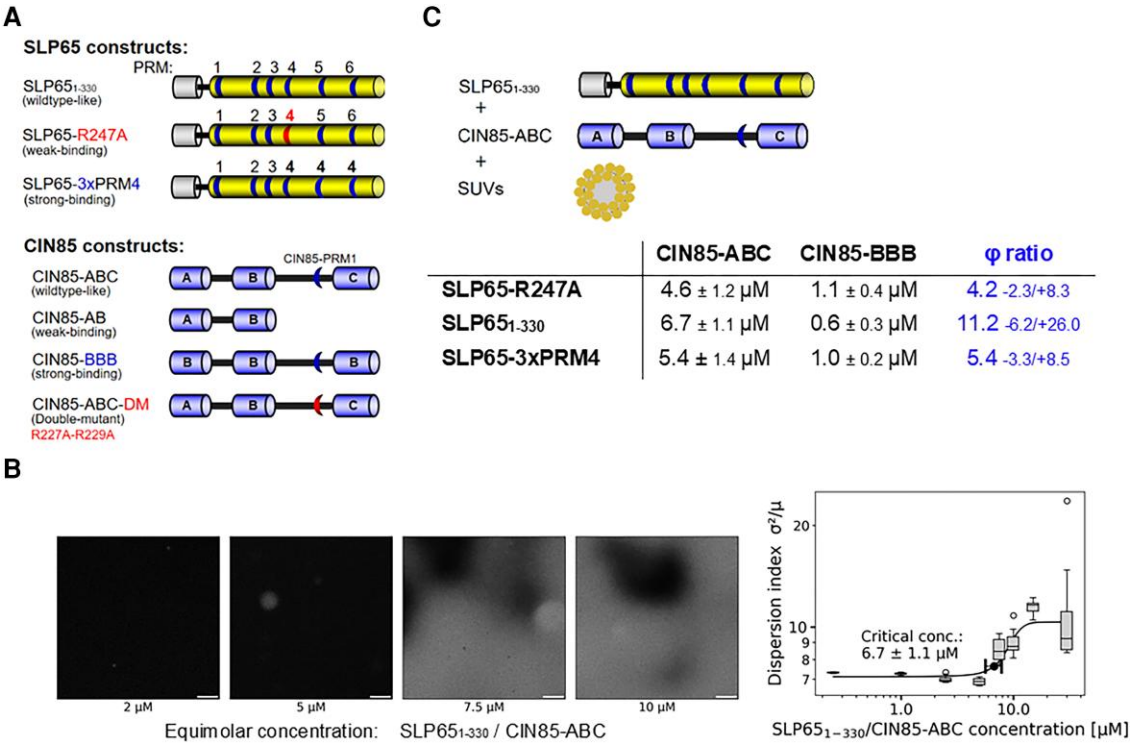

Fig. 2. Exploring the phase-separation behavior of the SH3–PRM system of CIN85 and SLP65. A) Construct design for weak- and strong-binding versions of SLP65 and CIN85. The $SLP65_{1\text{-}330}$ construct, shortened at the C-terminus comprising residues 1-330, lacks the C-terminal SH2 domain, which is irrelevant to the CIN85 interaction. The weak-binding SLP65-R247A construct has a reduced affinity to CIN85 due to the R247A mutation, which deactivates the binding of PRM4. The strong-binding SLP65-3xPRM4 construct is designed by replacing both PRM5 and PRM6 with PRM4. The CIN85-ABC comprises residues 1-333. The weak-binding CIN85-AB construct contains only SH3A and SH3B. In the strong-binding CIN85-BBB construct, the SH3A and SH3C domain are each replaced by the strong-binding SH3B domain. In the CIN85-ABC-DM construct the CIN85-PRM1 is deactivated by the R227A and R229A mutations. B) Experimental determination of the saturation concentration of phase separation: atto430LS-SLP65, CIN85, and SUV were mixed in a concentration series and imaged by confocal fluorescence microscopy. The saturation concentration is obtained by a sigmoidal fit of the dispersion index (ratio of the variance σ to the mean μ). C) Saturation concentrations of phase separation (ϕ_{exp}) of mixture compositions of SUV + CIN85 + SLP65 mixed at equimolar protein concentrations. The strong-binding version CIN85-BBB reduces ϕ_{exp} compared to the *wildtype*-like CIN85-ABC construct by a factor of 4 to 11, referred to as ϕ-ratio, whereas the weak- and strong-binding SLP65 versions, SLP65-R247A and SLP65-3×PRM4, respectively, have no effect on the saturation concentration for phase separation. The ϕ-ratio is given as the number and the confidence interval is given toward smaller and larger numbers. For example, 4.2 −2.3/+8.3 means that the confidence interval is from 4.2 − 2.3 = 1.9 to 4.2 + 8.3 = 12.5. D) Saturation concentrations of phase separation ϕ_{exp} of SLP65/CIN85 mixtures without SUVs. ϕ ratios are calculated as the ratio of the saturation concentrations of two different mixtures. ϕ_{exp} of the SLP65-R247A & CIN85-ABC mixture could not be fitted in our measurements with an upper end of the concentration series of 320 μM (SI Appendix, Fig. S9), N.m., not measured. The error for ϕ ratios is given as a confidence interval as in Fig. 1C.

spectra of the titration of SLP65-PRM6 to the ^{15}N-SH3A show most peaks in fast exchange, except for D16 and N51, which exhibit intermediate exchange (SI Appendix, Fig. S3A, marked by arrows). An illustrative example of intermediate exchange is the titration of SLP65-PRM4 to ^{15}N-SH3C (SI Appendix, Fig. S3B). The slow exchange was observed in the titration of SLP65-PRM4 to ^{15}N-SH3B (SI Appendix, Fig. S3C). Moreover, the K_Ds were determined by isothermal titration calorimetry (ITC) (SI Appendix, Fig. S4, upper panel). The measurements by ITC, as an independent technique, corroborated the K_Ds measured by NMR (Fig. 1C; SI Appendix, Fig. S5). Both methods, ITC and NMR, demonstrate that PRM4 is the strongest binding motif, followed in rank by PRM5 and PRM6, while PRM1 and PRM3 interact weaker. PRM2 was found to be the weakest binding motif, for which no heat release could be measured by ITC (SI Appendix, Fig. S4, lower panel).

The strong-binding CIN85-BBB, but not the SLP65-3xPRM4 construct reduces the saturation concentration for tripartite phase separation

Presignaling condensates composed of vesicle-associated SLP65 and CIN85 can be reconstituted in vitro by mixing recombinant

Downloaded from https://academic.oup.com/pnasnexus/article/3/3/pgae079/7607901 by Max-Planck Society user on 21 March 2024

SLP65, CIN85, and small unilamellar vesicles (SUVs) at physiological concentrations (14). In order to investigate how the dissociation constant influences phase separation, weak-, and strong-binding SLP65 and CIN85 constructs were designed (Fig. 2A) taking advantage of the previously determined dissociation constants (Fig. 1C). Specifically, we studied the effect of enhancing the interaction between SPL65 and CIN85 by introducing more or less of the strong PRM4/SH3B interactions. In one implementation with enhanced PRM4/SH3B interactions, the low-affine PRM5 and PRM6 were replaced by PRM4 leading to the SLP65-3xPRM4 construct. The second implementation to enhance the PRM4/SH3B interactions was the CIN85-3xSH3B construct, herein referred to as CIN85-BBB, in which each of the weaker binding SH3A and SH3C domains were replaced by the SH3B domain. On the other hand, to weaken the influence of the PRM4/SH3B interaction we used the SLP65-R247A construct that has a SH3 domain binding incompetent PRM4 due to the R247A mutation (20). Due to higher yield in recombinant protein production, the C-terminally shortened versions $SLP65_{1\text{-}330}$ and $CIN85_{1\text{-}333}$ were produced and used for measurements. $CIN85_{1\text{-}333}$ contains the SH3A, -B, and -C domains and is herein referred to as CIN85-ABC construct. We note that the CIN85-ABC construct does not trimerize, in contrast to full-length CIN85, which contains the C-terminal coiled-coil domain.

To elucidate the strength of binding of the described constructs, we measured their dissociation constants by ITC (SI Appendix, Table S1). *Wildtype* $SLP65_{1\text{-}330}$ and CIN85-ABC had a K_D of 1.36 ± 0.17 μM (SI Appendix, Fig. S6A) which dropped by a factor of almost 6 ($K_D = 0.24 \pm 0.01$ μM) when $SLP65_{1\text{-}330}$ was replaced by SLP65-3xPRM4 (SI Appendix, Fig. S6B). As expected, a larger K_D of 7.04 ± 1.12 μM was measured when $SLP65_{1\text{-}330}$ was replaced by SLP65-R247A (SI Appendix, Fig. S6C). The K_Ds of the interactions of the CIN85-BBB construct with either the $SLP65_{1\text{-}330}$ or the SLP65-3xPRM4 construct were 0.7 ± 0.25 and 0.14 ± 0.06 μM, respectively (SI Appendix, Fig. S6D and E) amounting to a change in K_Ds of around 2 when CIN85-ABC was replaced by CIN85-BBB (SI Appendix, Table S1). The interaction of CIN85-BBB with SLP65-R247A was found similar in strength to CIN85-ABC with SLP65-R247A (SI Appendix, Fig. S6C and F).

Subsequently, we explored the affinity-dependent phase-separation behavior of the tripartite system by confocal fluorescence microscopy, imaging mixtures of the described constructs of SLP65 and CIN85 at equimolar concentration with vesicles (Fig. 2B). Since in solution, SLP65/CIN85/vesicle condensates sink down just after mixing, the visualization of condensates on the bottom of the microscopy slide was preferred over turbidity measurements in a vial (31). The saturation concentration of phase separation (ϕ_{exp}) was determined by fitting the dispersion index (SI Appendix, Figs. S7 and S8), since it is a simpler method than dual-color fluorescence cross-correlation spectroscopy (32) and since it is a more objective measure than visual evaluation (33). For the measurements, SLP65 partially labeled with fluorescein (up to 10 μM) was used. The mixture of $SLP65_{1\text{-}330}$, CIN85-ABC, and SUVs resulted in ϕ_{exp} of 6.7 ± 1.1 μM (Fig. 2C; SI Appendix, Fig. S7A), while the weak-binding version SLP65-R247A mixed with CIN85-ABC and SUVs resulted in a lower ϕ_{exp} (4.5 ± 1.2 μM, SI Appendix, Fig. S7B). The strong-binding version SLP65-3xPRM4 with CIN85-ABC and SUVs delivered a ϕ_{exp} of 5.5 ± 1.4 μM (SI Appendix, Fig. S7C). Thus, inactivating PRM4 (SLP65-R247A) or increasing its number (SLP65-3xPRM4) had a marginal effect on ϕ_{exp}. In contrast, CIN85-BBB mixed with SUVs and either SLP65-R247A, $SLP65_{1\text{-}330}$ or SLP65-3xPRM4 resulted in ϕ_{exp}s of 1.1 ± 0.4, 0.6 ± 0.3, and 1.0 ± 0.2 μM, respectively (SI Appendix, Fig. S7D–F), all being lower by factors between 4 and 11 (ϕ ratios in Fig. 1C) compared to the ϕ_{exp} values measured with CIN85-ABC. Surprisingly, the CIN85-BBB construct, but not the SLP65-3xPRM4 construct, did promote tripartite phase separation, despite the fact, that SLP65 contains three strong-binding modules, too, and both constructs having a lower global K_D than the wildtype constructs ($SLP65_{1\text{-}330}$, CIN85-ABC) (SI Appendix, Table S1). This puts into evidence that neither individual K_Ds nor global K_Ds are predictive for saturation concentrations of phase separation. This poses the question of why the triplication of PRM4 does not have the same phase-separation promotion effect as the introduction of the triple SH3B construct.

Replacement of SH3C by SH3B promotes phase-separation properties of CIN85-BBB

As described above, the SLP65 mutants did not significantly shift the saturation concentration in the tripartite system, but the CIN85 mutants did. We set out to understand these properties by simulations with the program LASSI taking into account the ranking of the individual K_Ds. Since we could not implement vesicles in LASSI, we investigated the SLP65–CIN85 system without SUVs.

Previous reports show that larger ϕ_{exp}s are measured, when the vesicles, one of three essential components for the tripartite system, were omitted (14). The mixtures of $SLP65_{1\text{-}330}$ with CIN85-ABC resulted in ϕ_{exp} of 36 μM (Fig. 2D; SI Appendix, Fig. S8A), which is, as expected, larger than the ϕ_{exp} of 6.7 μM including SUVs (Fig. 2C). Next, we analyzed the effect of the constructs designed to enhance the SH3/PRM interaction. The mixture of SLP65-3xPRM4 with CIN85-ABC showed a larger ϕ_{exp} of 62 μM (Fig. 2D) demonstrating a weak effect of SLP65-PRM4. The weak-binding SLP65-R247A mutant did not phase separate with the CIN85-ABC construct up to equimolar concentrations of 280 μM (SI Appendix, Fig. S9), which confirms the relevance of PRM4 for CIN85 binding and corroborates previous findings regarding its role in CIN85 binding and Ca^{2+} signaling [cp. Fig. 3A in Oellerich et al (20)]. While the SLP65-R247A construct did not phase separate with CIN85-ABC, it did so when mixed with CIN85-BBB, resulting in a ϕ_{exp} of 12 μM (Fig. 2D; SI Appendix, Fig. S8E). $SLP65_{1\text{-}330}$ with CIN85-BBB resulted in ϕ_{exp} of 4 μM (Fig. 2D; SI Appendix, Fig. S8F) reproducing the previous finding that CIN85-BBB compared to CIN85-ABC promoted phase separation strongly (ϕ ratios "ABC/BBB" in Fig. 2C). Next, SLP65-3xPRM4 with CIN85-BBB resulted in ϕ_{exp} of 4 μM (Fig. 2D; SI Appendix, Fig. S8G) reproducing the modest effect of triplication of PRM4 as seen before in the presence of SUVs. In conclusion, the tripartite system yielded ϕ_{exp} values ranging from 0.6 to 6.7 μM (Fig. 2C), while the ϕ_{exp} of the two protein system ranged from 2.9 μM to above 260 μM (Fig. 2D). Replacing CIN85-ABC by CIN85-BBB induces the most dramatic reduction in saturation concentration of phase separation, yet the effects are quantitatively larger without SUVs than with (Fig. 2C and D). The replacement of $SLP65_{1\text{-}330}$ by SLP65-3xPRM4 had almost no effect in the presence of SUVs and a quantitatively much smaller effect without SUVs than replacement of CIN85-ABC by CIN85-BBB.

Parallel to these studies, a previously not described SH3 domain binding motif was identified in the linker between SH3B and SH3C, referred to here as CIN85-PRM1 (26). We were interested if whether CIN85-PRM1 could influence phase separation. The binary K_Ds of CIN85-PRM1 to SH3A, SH3B, and SH3C were

Downloaded from https://academic.oup.com/pnasnexus/article/3/3/pgae079/7607901 by Max-Planck Society user on 21 March 2024

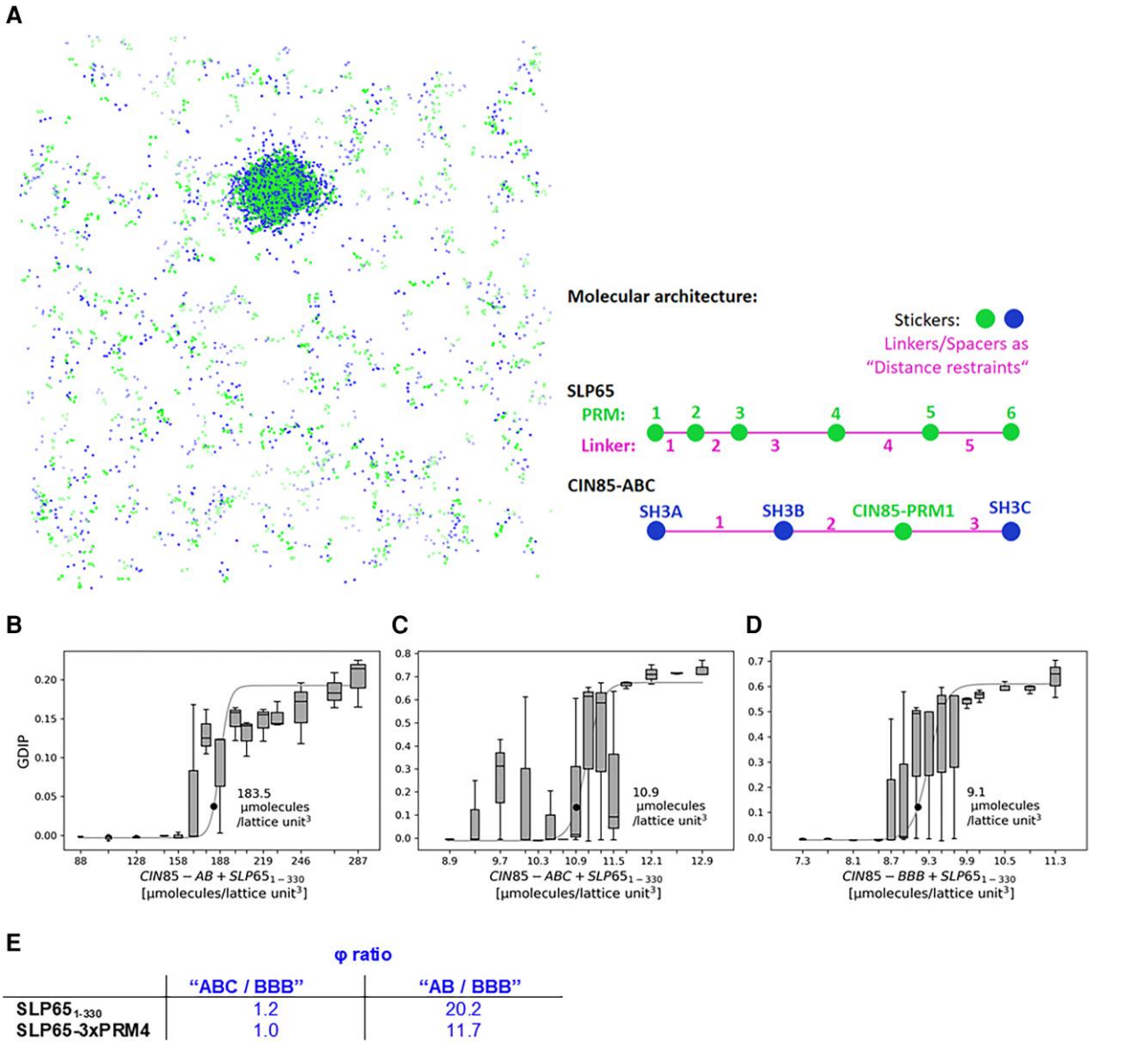

Fig. 3. Analysis of CIN85's and SLP65's phase separation by simulations of the saturation concentration ϕ_{sim}. A) LASSI simulations of the molecules' PRM_m–$SH3_n$ system to visualize the molecular cluster of the SH3 stickers (blue) and PRM stickers (green) of 1,000 *CIN85-BBB* molecules and 1,000 $SLP65_{1-330}$ molecules (2,000 simulated molecules in total). In this representative simulation, the condensates are simulated at 9.1 micromolecules per lattice-unit^3 and a spacer scaling = 1/6 (see main text). B to D) $SLP65_{1-330}$ was combined with either *CIN85-AB*, *CIN85-ABC*, or *CIN85-BBB*. ϕ_{sim} was obtained by fitting the GDIP. The simulations with *CIN85-AB* (B) have a significantly different ϕ_{sim} than *CIN85-ABC* (C) and *CIN85-BBB* (D). E) ϕ ratios of the simulations (deduced from SI Appendix, Fig. S13) with spacer scaling of 1/6).

720 ± 20, 1,140 ± 50, and 210 ± 10 µM as measured by NMR titration spectroscopy (Fig. 1C) (26). Since the SH3C domain is in close proximity to CIN85-PRM1, has the smallest K_D, and occupies fully the PRM binding site of SH3C, CIN85-PRM1 is expected to prevent binding of SH3C to SLP65 PRMs. Indeed, probing CIN85-AB with $SLP65_{1-330}$ resulted in a ϕ_{exp} of 18 µM (SI Appendix, Fig. S8C, 36 µM for CIN85-ABC, Fig. 2D) and with SLP65-3xPRM4 in a ϕ_{exp} of 32 µM (SI Appendix, Fig. S8D), 62 µM for CIN85-ABC, Fig. 2D. The absence of SH3C and its linker containing CIN85-PRM1 rather promotes phase separation at concentrations lower by a factor of 0.5 (Fig. 2D). In conclusion, in CIN85-ABC, SH3C appears deactivated, such that it behaves very similar to CIN85-AB. CIN85-BBB, however, engages all three SH3B domains in interactions with PRMs of SLP65 since SH3B is not deactivated by CIN85-PRM1.

Modeling of SLP65-CIN85 phase separation indicates that CIN85-ABC is effectively bivalent

We further elucidated the phase-separation behavior of the SLP65 and CIN85 constructs introduced above by computational modeling with the program LASSI in order to relate the individual K_Ds to the phase-separation behavior (29). The lattice-based Monte Carlo simulation uses stickers for which pairwise affinities can be defined and spacers that are neutral regarding binding (Fig. 3A). The SH3 domains of CIN85 and the PRMs of SLP65 constitute the stickers, whose interactions are defined by a sticker–sticker energy matrix parameterized by the experimentally determined ΔG values, derived from the K_D values (Fig. 1C; SI Appendix, Fig. S10). Spacers represent the intrinsically disordered regions between the SH3 domains in CIN85 and between the PRMs in SLP65.

Downloaded from https://academic.oup.com/pnasnexus/article/3/3/pgae079/7607901 by Max-Planck Society user on 21 March 2024

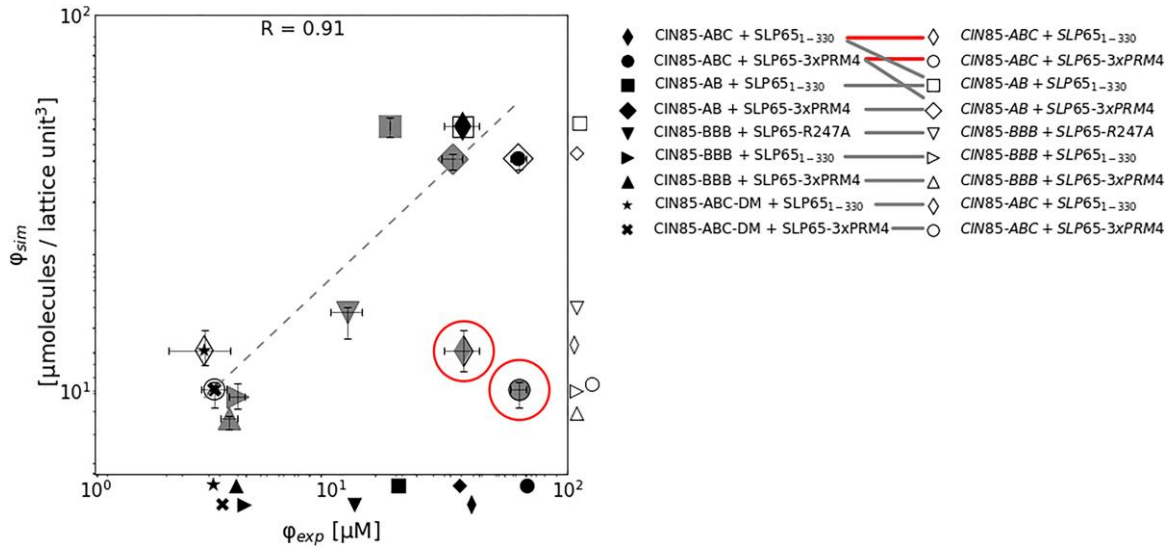

Fig. 4. Correlation plots of ϕ_{exp}- vs. ϕ_{sim}-values. *CIN85-AB* and *CIN85-BBB* correlate with CIN85-AB and CIN85-BBB, respectively. *CIN85-ABC* does not correlate with CIN85-ABC (circled red), but *CIN85-ABC* correlates with the CIN85-PRM1-inactivated CIN85-ABC-DM. The Pearson correlation coefficient is calculated from nine pairs of ϕ_{exp}- vs. ϕ_{sim}-values, excluding the correlations of CIN85-ABC + $SLP65_{1\text{-}330}$/SLP65-3xPRM4 with *CIN85-ABC* + $SLP65_{1\text{-}330}$/*SLP65-3xPRM4* (circled red) ϕ-values of simulations with the spacer scaling of 1/4 are shown.

For simulations of CIN85, we included in addition to the CIN85-ABC and CIN85-BBB construct also the CIN85-AB construct. This is due to the fact that LASSI modeling could not reproduce the experimentally found 100% occupancy of the intramolecular interaction between SH3C and CIN85-PRM1 (26). Thus, CIN85-ABC with its inactive SH3C domain is, therefore, best represented by CIN85-AB.

Hereinafter we represent constructs for simulation in *italic* while constructs in experiments are shown in normal font. As a starting point, the spacer lengths were calculated in the following way. The PRMs are six amino acids long and represent one sticker lattice point. Therefore, the number of amino acids for a spacer was divided by 6 (scaling factor 1/6) to obtain the number of lattice points for a spacer (e.g. a 60 amino acid long linker is scaled to a spacer length of 10). In order to evaluate the impact of the spacer length we varied the scaling factors between 1/2 and 1/10 (SI Appendix, Table S2). For illustration, the condensate of the simulation of *CIN85-BBB* with *SLP65* is visualized (Fig. 3A). The simulated saturation concentration (ϕ_{sim}) for phase separation was determined by fitting the global density inhomogeneity parameter (GDIP), which reports about the dispersion of the molecules. A GDIP value above 0.025 indicates phase separation (29). The ϕ_{sim} values of *SLP65* with *CIN85-AB*, *–ABC*, and *–BBB* are indicated as black point in Fig. 3B–D, respectively. In some simulations, a phase transition occurred at very high concentrations, where the GDIP was not suitable for our analysis anymore. In this case, the percolation value, defined as the fraction of polymers of the single largest cluster (29), was used to calculate the saturation concentration. In our simulations, the GDIP scales with the percolation value except for the simulations of $SLP65_{1\text{-}330}$ with *SH3-AB* (SI Appendix, Fig. S11).

The simulations of *CIN85-BBB* with either *SLP65* or *SLP65-3xPRM4* resulted in ϕ_{sim}s of 9.1 and 9.4 micromolecules per lattice-unit^3, respectively (SI Appendix, Fig. S13, scaling 1/6), which were similar to the ϕ_{sim} values of 10.9 and 9.5 micromolecules per lattice-unit^3 for *CIN85-ABC* and did, therefore, not match with the experimental observations in which CIN85-BBB lead to lower saturation concentration than CIN85-ABC or CIN85-AB (Fig. 2D). The experiment and the simulation of CIN85-ABC did not agree (Fig. 4, red circle). This nonmatching behavior is expected when in the experiment SH3C does not participate in the interaction with PRMs of SLP65. In line with the deactivation of SH3C by CIN85-PRM1, the experimental ϕ_{exp}-ratios of CIN85-AB vs. CIN85-BBB (4.4 and 8.8, Fig. 2D, colored blue) matched with the simulated ones (20.2 and 11.7, Fig. 3E) within factors of 4.6 and 1.3, respectively. Thus, CIN85-ABC can be modeled faithfully by *CIN85-AB*, i.e. omitting the SH3C interactions with the SLP65 PRMs due to the binding of CIN85-PRM1 to SH3C.

The intramolecular interaction of CIN85-PRM1 impairs SH3C's contribution to phase separation

The parameterized model showed a correlation of the simulated and experimental ϕ-values (Fig. 4, white and black symbols, respectively) of CIN85-AB and CIN85-BBB (squares and triangles, respectively). We further investigated the contribution of CIN85-PRM1 to phase separation. We engineered a construct with inactivated CIN85-PRM1 in order to test its effect experimentally. CIN85-PRM1 was deactivated in the CIN85 double mutant (CIN85-ABC-DM) by the R227A and R229A mutations (26), i.e. it should be faithfully modeled by *CIN85-ABC*. The mixtures of $SLP65_{1\text{-}330}$ with CIN85-ABC-DM (Fig. 4, black star) resulted in ϕ_{exp} of 2.9 μM (Fig. 2D; SI Appendix, Fig. S8H) and correlates with the simulated *CIN85-ABC* (Fig. 4, white diamond). In contrast, CIN85-ABC with $SLP65_{1\text{-}330}$ has a larger ϕ_{exp} of 36 μM and does not correlate with ϕ_{sim} (diamond in gray marked by the red circle), due to the CIN85 SH3C–PRM1 interaction not modeled in the LASSI simulations. ϕ_{exp} of CIN85-ABC-DM is indeed similar to the ϕ_{exp} of CIN85-BBB (Fig. 2D). This is recapitulated in the simulations: *CIN85-ABC* that ignores the intramolecular CIN85 SH3C–PRM1 interaction has a ϕ_{sim} of 10.9 similar to 9.1 of *CIN85-BBB* (SI Appendix, Fig. S13). Similar to $SLP65_{1\text{-}330}$ with CIN85-ABC-DM (2.9 μM, SI Appendix, Fig. S8H), the mixture of SLP65-3xPRM4 with CIN85-ABC-DM has a ϕ_{exp} of 3.2 μM (SI Appendix, Fig. S8I), which also agrees with the LASSI simulation: 9.5 for *CIN85-ABC*

Downloaded from https://academic.oup.com/pnasnexus/article/3/3/pgae079/7607901 by Max-Planck Society user on 21 March 2024

with *SLP65-3xPRM4* and 9.4 for *CIN85-BBB* with *SLP65-3xPRM4* (Fig. 4). The correlations were consistent with varying linker length scaling (SI Appendix, Figs. S13 and S14). In summary, the mixtures of the CIN85-ABC-DM construct phase separated at saturation concentrations similar to the mixtures of the CIN85-BBB construct (Fig. 4, bottom left part of the diagram), while the bivalent CIN85-AB construct and the CIN85-ABC construct have more similar phase-separation properties (Fig. 4, upper right part) due to the deactivation of SH3C by CIN85-PRM1. CIN85-ABC-DM and the CIN85-BBB constructs are trivalent, whereas the CIN85-AB is bivalent and CIN85-ABC acts like a bivalent molecule. Supported by the LASSI model, the experiments demonstrate that valency is a major determinant for CIN85's phase separation. This finding is in line with earlier studies, which revealed that phase separation of multivalent proteins is primarily governed by valency (28, 34–36), while further determinants driving phase separations such as affinity (37) and linker length (38, 39) are secondary.

Conclusions

LASSI has been successfully applied to biological systems like IDPs (35), poly-SH3/poly-PRM-type (38), and multiphase systems (40). We applied the LASSI program to the natural multivalent system of the SLP65-CIN85 complex, and described its phase-separation process emerging from natural, promiscuous PRM–SH3 sticker interactions. The phase-separation concentrations could be predicted from the individual dissociation constants of the individual components faithfully and variations of composition were described correctly by the LASSI simulations. LASSI was further used as a heuristic tool to detect previously undetected interactions: while analyzing the affinity-dependent SLP65/CIN85 phase separation, we noticed a discrepancy between the simulated and measured saturation concentrations of the CIN85-ABC constructs (Fig. 4, circled red). This was in line with the identification of bivalency in CIN85-ABC, where SH3C was deactivated by intramolecular binding to CIN85's PRM1. These findings highlight the impact of valency on the saturation concentration, as was described before in pioneering studies by Li et al. (28). Moreover, the simulations comprehensibly describe configurations of a phase-separated, large molecular cluster at a protein domain level resolution.

Materials and methods

Reagents

Peptide synthesis and vesicle preparation, as well as protein production, can be found in the SI Appendix, Material and methods.

Biophysical interaction studies

NMR and ITC titration experiments are described in the SI Appendix.

Fluorescence microscopy assay and image analysis

Sample preparation was performed as described previously (14). Briefly, the protein constructs were mixed with or without SUVs in 1.5 mL reaction tubes (Eppendorf). The total volume of each mixture was 25 µL. For a robust assay, the components were added in distinct order, starting with the addition of buffer (20 mM 2-(4-(2-hydroxyethyl)-1-piperazinyl)-ethanesulfonic acid (HEPES) pH 7.2, 100 mL NaCl). Then, the atto430LS-labeled SLP65 construct, the unlabeled SLP65 construct, and the CIN85 construct were added sequentially. For mixtures including SUVs, an SUV stock solution with 5 mM lipid concentration was pipetted to the buffer first, and then the protein constructs were pipetted. The mixtures were transferred into the wells of a microscopy slide (uncoated µ-slide 8 well, ibidi GmbH, Gräfelfing). Before imaging, phase-separated droplets were allowed to settle on the surface during an incubation time of 45–75 min. The phase separation of mixtures with SLP65, CIN85, and SUVs was imaged with a Zeiss LSM780 confocal microscope equipped with an MBS 458 beam splitter and a Plan-Apochromat 40×/1.4 Oil DIC M27 objective. To image the settled dense phase right above the bottom of the well, a 4–8 µm z-stack with a step size of 1 µm was acquired. Atto 430LS-labeled SLP65 was excited by an argon laser at 458 nm. Emission was detected in the 520–600 nm range. Laser settings and representative acquisition parameters were chosen depending on the fluorophore concentration. For quantification and to avoid intensity saturation of the image, not more than 10 µM atto430LS-labeled SLP65 was used. In parallel, bright field (BF) images were recorded (detector gain BF: 400). Images of the surface (z-position at ∼0 µm) were selected and analyzed with the ImageJ software (NIH, Bethesda, MD, USA). The dispersion index σ^2/μ was calculated from 16-bit images ($n = 15$), where σ is the variance and μ the mean of the pixel intensities. The saturation concentration ϕ_{exp} for phase separation was obtained by fitting the dispersion index to the logistic function $DI = \frac{H}{1+e^{-k(x-x_0)}} + C$, where H, C, and k are scaling parameters of which H and C depend on the absolute signal intensity, x_0 is a location parameter, and ϕ_{exp} is defined as the maximum of the second derivative of the fit.

Computational model

In the applied LASSI model (29), the definitions of SLP65's and CIN85's molecular architecture are described in the main text (Fig. 3) and illustrated in Table S2 (SI Appendix). The simulations included in total of 2,000 molecules (1,000 for each SLP65 and CIN85) in order to avoid finite-size effects (29). Rotational, local, colocal, shake, translation, small cluster translation, cluster translation, pivot, and double pivot moves were applied at frequencies of 0.25, 0.13, 0.25, 0.04, 0.04, 0.04, 0.04, 0.13, and 0.10 per step considering the suggestions for the settings from the authors (29). The anisotropic interaction energy terms were experimentally parametrized by the Gibbs free energy ΔG (SI Appendix, Fig. S10) in terms given by $\Delta G = -RT \ln(1/K_D)$, with the dissociation constant K_D, the temperature $T = 310$ K, and the gas constant $R = 1.987$ cal mol^{-1} K^{-1}. The isotropic interaction energy terms were set to zero to allow for simulations with short linker lengths as suggested by the authors of LASSI (personal correspondence). 2×10^9 Monte Carlo steps were run in order to approach apparent convergence of the simulation. To simulate the saturation concentration, a set of simulations was performed, in which the concentration was varied by reducing the box size. In the rectangular cuboid box, the simulated concentration is given in units of micromolecules per lattice-unit^3, which represents 10^{-6} molecules per lattice-unit^3, with 2,000 molecules and a box size length between 85 and 900 lattice units. The radial density distribution (provided by the software) was normalized with the a priori radial density distribution (simulations with zero energy interaction terms). The GDIP was calculated from the normalized radial density distribution function for each simulation. The saturation concentration was obtained by fitting the GDIP of three simulations ($n = 3$). Bootstrap errors were calculated for the simulated and experimentally determined saturation concentration with 5,000 repetitions. For each repetition, 15 dispersion index values or three GDIP values of the sample data were randomly

Downloaded from https://academic.oup.com/pnasnexus/article/3/3/pgae079/7607901 by Max-Planck Society user on 21 March 2024

chosen per concentration point, and fitted to obtain the saturation concentration. The standard deviation was calculated from the list of the saturation concentrations.

Acknowledgments

We thank Claudia Schwiegk and Kerstin Overkamp for excellent technical help and peptide synthesis. We thank Ángel Pérez-Lara for assistance with ITC experiments and the Live-cell imaging facility at the MPI for Multidisciplinary Sciences for access to the microscopes.

Supplementary Material

Supplementary material is available at *PNAS Nexus* online.

Funding

This project was supported by the DFG (Deutsche Forschungsgemeinschaft) in the framework of the SFB860 and by the MPG (Max Planck Gesellschaft).

Author Contributions

J.M., S.B., and C.G. designed research; J.M., D.S., and L.E.W. performed research; J.M., D.S., and F.D. analyzed data; J.W. and C.G. secured the funding for the research; J.M., S.B., D.S., J.W., and C.G. wrote the paper; S.B. contributed reagents.

Preprints

A preprint is deposited on bioRxiv. The copyright holder for this preprint is the author/funder, who has granted bioRxiv a license to display the preprint in perpetuity. All rights reserved. No reuse is allowed without permission. This manuscript was posted on a preprint: 10.1101/2023.07.31.551239.

Data Availability

The processed data that support the findings of this study are included in the article and Supplementary material. The raw data are deposited on Figshare https://doi.org/10.6084/m9.figshare.25204064.

References

1 Hyman AA, Brangwynne CP. 2011. Beyond stereospecificity: liquids and mesoscale organization of cytoplasm. *Dev Cell*. 21(1):14–16.
2 Banani SF, *et al.* 2017. Biomolecular condensates: organizers of cellular biochemistry. *Nat Rev Mol Cell Biol*. 18(5):285–298.
3 Han TW, *et al.* 2012. Cell-free formation of RNA granules: bound RNAs identify features and components of cellular assemblies. *Cell*. 149(4):768–779.
4 Kato M, *et al.* 2012. Cell-free formation of RNA granules: low complexity sequence domains form dynamic fibers within hydrogels. *Cell*. 149(4):753–767.
5 Nott TJ, *et al.* 2015. Phase transition of a disordered nuage protein generates environmentally responsive membraneless organelles. *Mol Cell*. 57(5):936–947.
6 Mittag T, Parker R. 2018. Multiple modes of protein-protein interactions promote RNP granule assembly. *J Mol Biol*. 430(23):4636–4649.
7 Uversky VN. 2021. Recent developments in the field of intrinsically disordered proteins: intrinsic disorder-based emergence in cellular biology in light of the physiological and pathological liquid-liquid phase transitions. *Annu Rev Biophys*. 50:135–156.
8 Hughes MP, *et al.* 2018. Atomic structures of low-complexity protein segments reveal kinked beta sheets that assemble networks. *Science*. 359(6376):698–701.
9 Van Treeck B, Parker R. 2018. Emerging roles for intermolecular RNA-RNA interactions in RNP assemblies. *Cell*. 174(4):791–802.
10 Wiedner HJ, Giudice J. 2021. It's not just a phase: function and characteristics of RNA-binding proteins in phase separation. *Nat Struct Mol Biol*. 28(6):465–473.
11 Peran I, Mittag T. 2020. Molecular structure in biomolecular condensates. *Curr Opin Struct Biol*. 60:17–26.
12 Milovanovic D, *et al.* 2018. A liquid phase of synapsin and lipid vesicles. *Science*. 361(6402):604–607.
13 Su X, *et al.* 2016. Phase separation of signaling molecules promotes T cell receptor signal transduction. *Science*. 352(6285):595–599.
14 Wong LE, *et al.* 2020. Tripartite phase separation of two signal effectors with vesicles priming B cell responsiveness. *Nat Commun*. 11(1):848.
15 Chong PA, Forman-Kay JD. 2016. Liquid-liquid phase separation in cellular signaling systems. *Curr Opin Struct Biol*. 41:180–186.
16 Xiao Q, McAtee CK, Su X. 2022. Phase separation in immune signalling. *Nat Rev Immunol*. 22(3):188–199.
17 Wienands J, *et al.* 1998. SLP-65: a new signaling component in B lymphocytes which requires expression of the antigen receptor for phosphorylation. *J Exp Med*. 188(4):791–795.
18 Fu C, *et al.* 1998. BLNK: a central linker protein in B cell activation. *Immunity*. 9(1):93–103.
19 Engelke M, *et al.* 2014. Macromolecular assembly of the adaptor SLP-65 at intracellular vesicles in resting B cells. *Sci Signal*. 7(339):ra79.
20 Oellerich T, *et al.* 2011. The B-cell antigen receptor signals through a preformed transducer module of SLP65 and CIN85. *EMBO J*. 30(17):3620–3634.
21 Pappu R, *et al.* 1999. Requirement for B cell linker protein (BLNK) in B cell development. *Science*. 286(5446):1949–1954.
22 Minegishi Y, *et al.* 1999. An essential role for BLNK in human B cell development. *Science*. 286(5446):1954–1957.
23 Keller B, *et al.* 2018. Germline deletion of CIN85 in humans with X chromosome-linked antibody deficiency. *J Exp Med*. 215(5):1327–1336.
24 Kühn J, *et al.* 2016. The adaptor protein CIN85 assembles intracellular signaling clusters for B cell activation. *Sci Signal*. 9(434):ra66.
25 Engels N, Wollscheid B, Wienands J. 2001. Association of SLP-65/BLNK with the B cell antigen receptor through a non-ITAM tyrosine of Ig-alpha. *Eur J Immunol*. 31(7):2126–2134. https://doi.org/10.1002/1521-4141(200107)31:7<2126::aid-immu2126>3.0.co;2-o.
26 Sieme D, *et al.* 2023. Autoinhibition in the Signal Transducer CIN85 Modulates B Cell Activation. bioRxiv 551229. https://doi.org/2023.07.31.551229 [accessed 2023 Aug 18].
27 Waudby CA, *et al.* 2016. Two-dimensional NMR lineshape analysis. *Sci Rep*. 6:24826.
28 Li P, *et al.* 2012. Phase transitions in the assembly of multivalent signalling proteins. *Nature*. 483(7389):336–340.
29 Choi JM, Dar F, Pappu RV. 2019. LASSI: a lattice model for simulating phase transitions of multivalent proteins. *PLoS Comput Biol*. 15(10):e1007028.
30 Bremer A, *et al.* 2022. Deciphering how naturally occurring sequence features impact the phase behaviours of disordered prion-like domains. *Nat Chem*. 14(2):196–207.

Downloaded from https://academic.oup.com/pnasnexus/article/3/3/pgae079/7607901 by Max-Planck Society user on 21 March 2024

31 Lin Y, Currie SL, Rosen MK. 2017. Intrinsically disordered sequences enable modulation of protein phase separation through distributed tyrosine motifs. *J Biol Chem*. 292(46): 19110–19120.
32 Peng S, *et al*. 2020. Phase separation at the nanoscale quantified by dcFCCS. *Proc Natl Acad Sci U S A*. 117(44):27124–27131.
33 Schutz S, Noldeke ER, Sprangers R. 2017. A synergistic network of interactions promotes the formation of in vitro processing bodies and protects mRNA against decapping. *Nucleic Acids Res*. 45(11): 6911–6922.
34 Banjade S, Rosen MK. 2014. Phase transitions of multivalent proteins can promote clustering of membrane receptors. *Elife*. 3: e04123.
35 Martin EW, *et al*. 2020. Valence and patterning of aromatic residues determine the phase behavior of prion-like domains. *Science*. 367(6478):694–699.
36 Ranganathan S, Shakhnovich E. 2019. Liquid-liquid microphase separation leads to formation of membraneless organelles. bioRxiv 881565. https://doi.org/2019.12.18.881565 [accessed 2023 Aug 18].
37 Errington WJ, Bruncsics B, Sarkar CA. 2019. Mechanisms of noncanonical binding dynamics in multivalent protein-protein interactions. *Proc Natl Acad Sci U S A*. 116(51): 25659–25667.
38 Harmon TS, *et al*. 2017. Intrinsically disordered linkers determine the interplay between phase separation and gelation in multivalent proteins. *Elife*. 6:e30294.
39 Sorensen CS, Kjaergaard M. 2019. Effective concentrations enforced by intrinsically disordered linkers are governed by polymer physics. *Proc Natl Acad Sci U S A*. 116(46):23124–23131.
40 Feric M, *et al*. 2016. Coexisting liquid phases underlie nucleolar subcompartments. *Cell*. 165(7):1686–1697.

Downloaded from https://academic.oup.com/pnasnexus/article/3/3/pgae079/7607901 by Max-Planck Society user on 21 March 2024